JACS
JOURNAL OF THE AMERICAN CHEMICAL SOCIETY
pubs.acs.org/JACS
Article

Deep Quantum-Dot Arrays in Moiré Superlattices of Non-van der Waals Materials

Zhigang Song,[#] Yu Wang,[#] Haimei Zheng, Prineha Narang,[*] and Lin-Wang Wang[*]

Cite This: J. Am. Chem. Soc. 2022, 144, 14657−14667
Read Online
ACCESS | Metrics & More | Article Recommendations | Supporting Information

ABSTRACT: Recently, moiré superlattices of twisted van der Waals (vdW) materials have attracted substantial interest due to their strongly correlated properties. However, the vdW interlayer interaction is intrinsically weak, such that many desired properties can only exist at low temperature. Here, we theoretically predict some unusual properties stemming from the chemical bonding between twisted PbS nanosheets as an example of non-vdW moiré superlattices. The strong interlayer coupling in such systems results in giant strain vortices and dipole vortices at the interface. The modified electronic structures become a series of dispersionless bands and artificial-atom states. In real space, these states are analogous to arrays of well-positioned quantum dots, which may be promising for use in single-electron devices. In theory, if the materials are doped with a low concentration of electrons, a Wigner crystal will form even without any magnetic field. To confirm the accessibility and stability of non-vdW moiré superlattices in experiment, we synthesized PbS moiré superlattices with different twist angles. Our transmission-electron-microscope observations reveal the resemblance of the small-angle-twisted structures with the square matrices of quantum dots, which is in good accordance with our calculations.

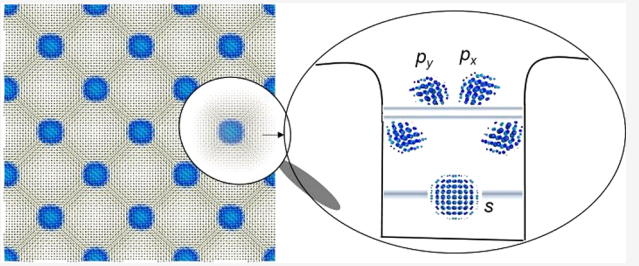

1. INTRODUCTION

Quantum dot arrays represent an exciting topic of interest to the physics, chemistry, and nanoscience communities. These systems have a variety of potential applications, such as semiconductor-quantum-dot qubits, solid-state memories, and single-photon sources.[1−3] However, the fluctuation of size, orientation, and separation distance during the synthesis of quantum dot arrays are major challenges for device upscaling. Previous attempts have been unable to produce identical quantum dots.[4,5] Moiré superlattices of twisted two-dimensional (2D) materials offer a novel pathway for overcoming these challenges as they naturally form a series of equally spaced, localized quantum states.[6,7] The distance between the quasi quantum dots may be tuned by adjusting the twist angle between the two sheets. This tunability allows moiré superlattices to be used in quantum information applications, for example, in simulations of the Hubbard model.[8,9]

Until now, research on moiré superlattices has focused on twisted van der Waals (vdW) bilayers or few layers. The interlayer interaction introduces a long-wavelength modulating potential on the electronic structure and vibrational properties. However, this modulating vdW interaction is weak, and the energy splitting of possibly flat bands is very small. For example, the energy splitting of flat bands in twisted bilayer graphene and twisted transition-metal dichalcogenides (TMDs) is only tens of millielectronvolts (meV) according to previous DFT (density functional theory) calculations.[10−15] This small energy splitting between the flat bands makes these weakly localized electron states susceptible to being destroyed by thermal fluctuations at room temperature, unlike quantum dot arrays which can have localized states at room temperature.[16,17] Despite the existence of strongly correlated phenomena in vdW moiré superlattices, they are usually observed at low temperatures,[18−20] such as below the superconductivity critical temperatures of (1.7 K) or the Mott insulating transition temperature (4 K) in magic-angle graphene.[21,22] After summarizing the recent progress in twistronics, a recent review pointed out that non-vdW materials may be a promising new direction in twistronics.[8] However, reports on the non-vdW moiré superlattices in both theory and experiments are rare because the fabrication has been thought to be impossible for a long time.

If, however, moiré superlattices can be fabricated using non-vdW materials, the interlayer modulating potential could be increased significantly due to much stronger interlayer interactions.[23] Large energy splitting and ultraflat electronic bands are expected.[24] The substantial atomic rearrangement can lead to shear solitons and topological point defects.[25−28]

Received: April 24, 2022
Published: August 3, 2022

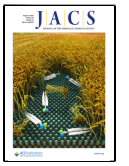

https://doi.org/10.1021/jacs.2c04390
J. Am. Chem. Soc. 2022, 144, 14657−14667

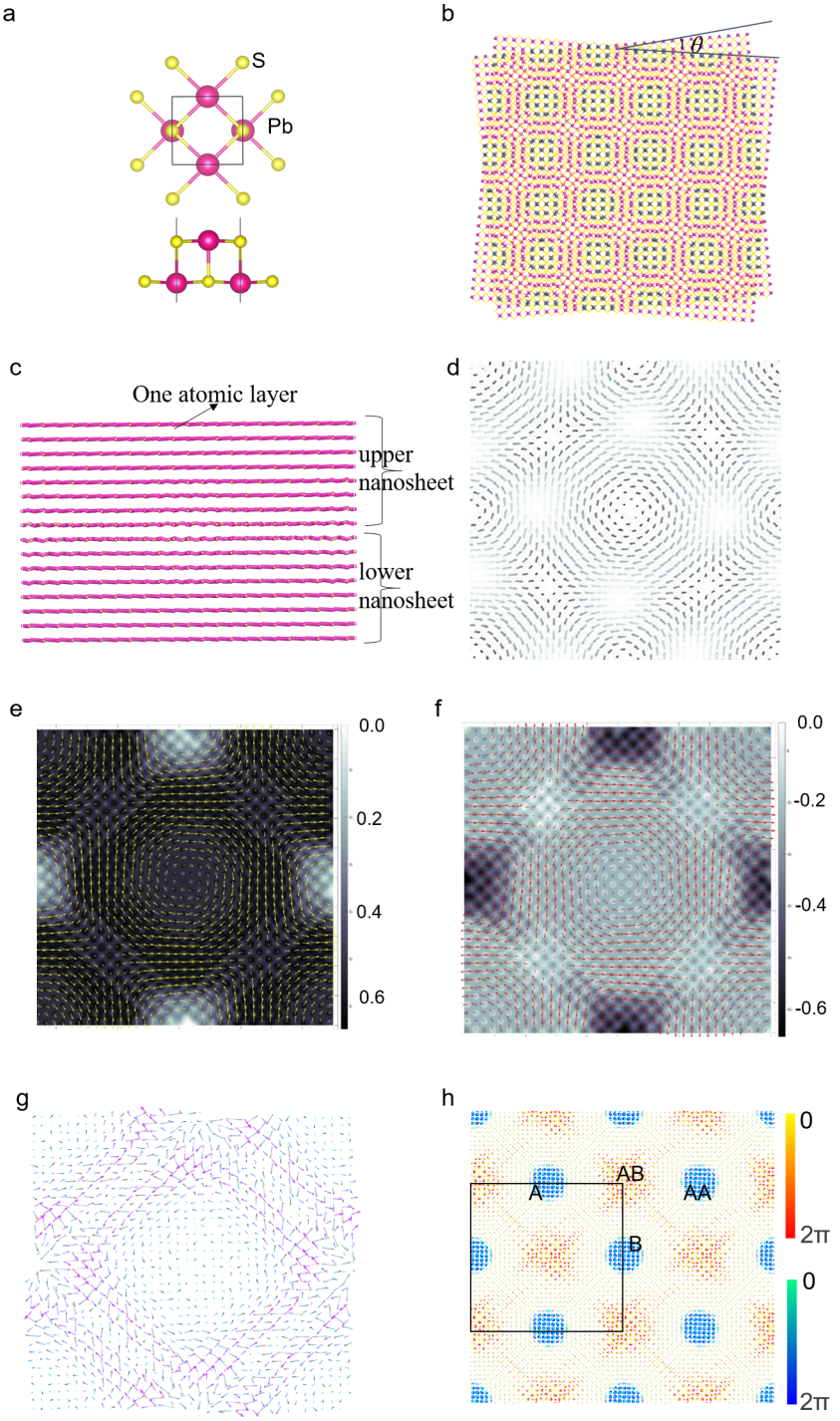

Figure 1. DFT calculation of PbS twisted layers. (a) Top and side views of the atomic structure of PbS layers. (b) Schematic of twisted PbS nanosheets and quantum dots. (c) Side view of twisted nanosheets of eight atomic layers. The twist angle is 3.47°. Red and yellow balls are lead and sulfur atoms, respectively. (d) Analytical results of the atomic displacement. (e,f) Atomic displacement at the upper and lower nanosheets. The color map represents the out-of-plane atomic reconstruction. Arrows represents the in-plane displacement. (g) Electric dipoles of the upper nanosheet at the interface. (h) Isosurface of charge density of the maximum unoccupied and minimum occupied states at the Γ point. The color represents the phase of a wave function. Square frame implies a moiré supercell.

Based on the strong localization, some novel devices, for example, single-electron devices, can be designed.[29,30] In addition, expanding the energy scale of interlayer interactions and band splitting can open doors to new fields to be explored. For example, quantum information dominates on the scale of 1 meV energy-level splitting. On the scale of tens of meV, THz electromagnetics is widely investigated. In the range of a few hundred to thousands of meV (characterized by the band gap of a semiconductor), optical and semiconducting properties are particularly important. Moiré superlattices with non-vdW interlayer coupling are able to function on the energy scale of a few hundred meV. Thus, despite the similarity in atomic structure, twisted non-vdW and vdW layers may have completely different applications.

https://doi.org/10.1021/jacs.2c04390
J. Am. Chem. Soc. 2022, 144, 14657−14667

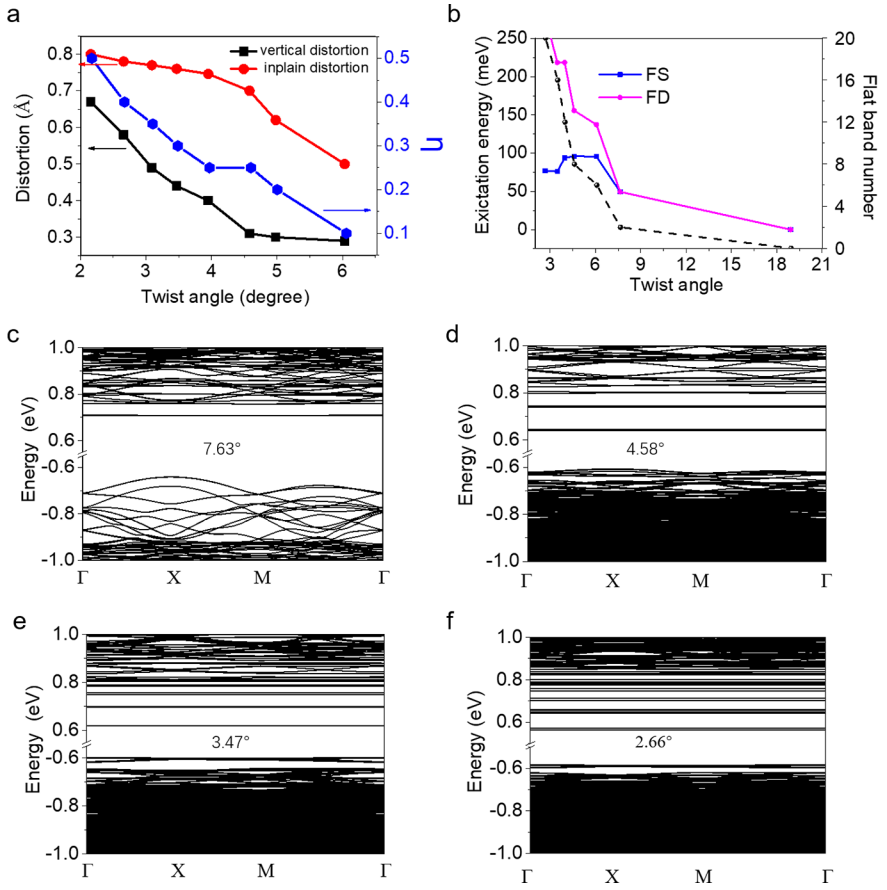

Figure 2. Electronic structure of twisted nanosheets. (a) Red and black are the maximum in-plane distortion (γ) and maximum distortion vertical to the plane as functions of twist angle. Blue is the asymmetry parameter of vortices (η) as a function of twist angle. (b) Excitation energy as a function of the twist angle in a unit cell. Blue corresponds to the excitation from the first to second flat bands (FS). Magenta corresponds to the excitation from the first flat band to the dispersed bands (FD). Dashed and black curve represent the number of flat bands inside an AA-stacked quantum dot. (c–f) Band structures with twist angles of 7.63°, 4.58°, 3.47°, and 2.66°, respectively. All energies are relative to the Fermi level.

The large splitting between flat bands corresponds to a deep trapping potential in real space, which leads to exotic electronic states on a small spatial scale and at high temperatures.[31] Among all of the interesting physical phenomena, one is the generalized Wigner crystal, i.e., the crystal of electrons. Wigner crystals were proposed decades ago[32] and have been probed in different systems, such as quantum Hall systems, modified quantum wires, as well as vdW moiré superlattices.[33−36] Usually, the trapping potential resulting from the splitting of Landau levels and the flat band splitting is very small, and therefore, the Wigner crystalline is susceptible to disorder and thermal fluctuation. As a result, Wigner crystallinity can only be detected at ultralow temperatures below 10 K, and even down to several mK in some cases.[37,38] Due to the deep trapping potential in real space, non-vdW moiré superlattices will be an ideal platform to probe various phases of generalized Wigner crystal.

In this work, we attempt to fill the gap of strongly coupled twisted layers through large-scale first-principles calculations combined with experimental synthesis and transmission electron microscope (TEM) observations. We begin with our *ab initio* calculations-based predictions of flat bands with atomic orbital-like wave functions that are energetically well separated from the bulk electronic bands. The energy splitting of flat bands in non-vdW materials is as large as a few hundred meV. Based on the extended Hubbard model, after suitable electron doping, the charge can be well-trapped in "quantum dots", forming a Wigner crystal without a magnetic field. Estimated by the thermal excitation and the band splitting, the possible Wigner crystal should be robust even at room temperatures. To experimentally confirm the possibility and stability of these unusual atomic structures, we synthesized PbS moiré superlattices with different twist angles. The TEM observations of superlattices are in good agreement with the DFT calculations. Non-vdW materials represent a major component of the aggregate materials landscape, the conclusion we present here are also applicable for other non-vdW materials to form new moiré superlattices.

2. RESULTS AND DISCUSSION

2.1. Theoretical Analysis. Conventionally, twisted superlattices consist of bilayers or few layers of van der Waals 2D layered materials, such as graphene or MoS_2.[39] In contrast to these layered materials, lead sulfide (PbS) has a nonlayered rock-salt 3D crystal structure in which atoms are connected through chemical bonding. Unlike vdW materials, nonlayered 3D materials generally cannot be peeled into 2D layers; however, 2D structures of nonlayered materials can be fabricated through chemical synthesis. Here, we study ultrathin nanosheets of PbS as a model system of nonlayered materials. We first calculated the band gap of single nanosheets with different atomic layers. Among them, the thinnest and most

https://doi.org/10.1021/jacs.2c04390
J. Am. Chem. Soc. 2022, 144, 14657−14667

stable PbS nanosheet is the one consisting of two atomic layers (Figure 1a). As shown in Figure S1, the band gap decreases from 1.84 to 0.53 eV as the number of atomic layers increases from 2 to infinity. Such PbS nanosheets are in the (001) surface direction. No surface passivation is needed, and there are no in-gap states on such unpassivated thin layers.

We then built moiré superlattices by commensurately twisting two nanosheets, as illustrated in Figure 1b.[40,41] We performed self-consistent DFT calculations to fully relax the twisted structures, which contain up to approximately 18000 atoms. The results with a twist angle of 3.47° are shown in Figure 1c. The side view reveals that the atomic reconstruction is mainly at the interface and its vicinity. Away from the interface, the atomic reconstruction decays fast. At 8 layers from the interface, the structure is approximated to the bulk structure with imperceptible distortions (details shown in Figure S2).

Due to the high computational cost, our DFT calculations mainly focus on twisted nanosheets in which each nanosheet consists of two atomic layers. An example of the 3.47° twist angle is shown in Figure 1e,f. Here, we find that the maximum out-of-plane atomic displacement has a value of 0.76 Å. Meanwhile, the in-plane atomic displacement is found to have a maximum value of 0.44 Å. Both the in-plane and out-of-plane displacements are much larger than the corresponding atomic arrangements in twisted bilayer graphene. Although strain patterns due to the out-of-plane reconstruction have been observed for twisted bilayer graphene and twisted transition-metal dichalcogenides,[42−44] it is difficult to observe in-plane displacement of twisted bilayer graphene in experiment since the in-plane displacement is smaller than 0.08 Å.[45] At the center of AB stacking in the relaxed structure, the atom distance between Pb and S is about 0.312 nm, which is in good agreement with the bonding length (0.301 nm) of Pb and S in bulk PbS. The distance would be around 0.41 nm if those two atoms are connected by the vdW interactions.[46] Besides, we can estimate the bonding energy using DFT calculations. The calculated bonding energy is around 0.28 eV/bond, much larger than the typical vdW interaction (usually below 0.1 eV/bond).[47] For example, vdW bonding energy is about 0.03 eV/bond in graphite.[48]

The significant reconstruction in twisted PbS layers allows us to study their symmetry and related properties. Figure 1e,f shows the in-plane and out-of-plane reconstruction for the upper and lower nanosheets at the interface. The out-of-plane displacement results in a series of strain bulbs, while the in-plane displacement results in a series of vortices. These vortices are topologically nontrivial in real space, and they are similar to Skyrmions in magnetic systems.[49] Their chirality in the upper and lower nanosheets is opposite. We find that the in-plane components of atomic displacement are well fitted by a simple sine function as $u(x, y) = \tau\gamma\ (-\sin(y + \eta \sin(y)), \sin(x + \eta \sin(x)))$ as shown in Figure 1d. γ and η are parameters characterizing the reconstruction strength and the inhomogeneity, respectively. $\tau = \pm 1$ is the layer index. In this example, $\gamma = 0.44$ Å and $\eta = 0.3$ for 3.47° twist angle. Both of these two parameters are dependent on the twist angle (as shown in Figure 2a). As the twist angle decreases, the in-plane reconstruction increases; i.e., both parameters increase. Similarly, the vertical distortion also increases as the twist angle decreases, but it saturates up to 0.80 Å. Interestingly, the electric dipoles at the interface also have a vortex structure as shown in Figure 1g. The chirality of the dipole vortices is opposite between the upper and lower nanosheets. The vortices of electric dipoles have been long-sought-after in both experiment and theory.[50−52]

The calculated band structures of twisted nanosheets are shown in Figure 2c−f. As the twist angle decreases, the calculated band gap decreases from 1.6 to 1.2 eV. The atomic reconstruction plays a very important role as shown in Figure S3. To show the importance of the atomic reconstruction, we performed geometry optimization with a twist angle of 7.6° followed by a band structure calculation of just one of the nanosheets with its reconstructed atomic configuration. Interestingly, we find that this single reconstructed nanosheet contains flat bands, while a regular single nanosheet does not contain any flat bands. These illustrative calculations demonstrate how the atomic reconstruction that results the interaction between the layers imprints the moiré structure on each nanosheet. If relaxation is not included in the twisted bilayers, the band gap is only about 0.7 eV, which is smaller than the band gap in the relaxed structure by about 0.6 eV. Thus, the relaxation is critical to the band structures and cannot be neglected. Referenced to the vacuum, the values of valence band maxima (VBM) and conduction band minima (CBM) will change after the upper layer and down layers in a unit cell have an interlayer shift. In previous literature, the largest energy difference of VBM (CBM) among different stacking configurations is approximated as the potential depth for VBM (CBM) states.[10,53,54] In this work, the maximum energy difference of CBM and VBM are found to be 0.2 and 0.157 eV, respectively (see Figure S4).

As the twist angle decreases, the bandwidth near the Fermi level becomes smaller and smaller. When the twist angle is smaller than 7.6°, the first "flat band" with a bandwidth of about 5 meV appears in the conduction bands. As the twist angle further decreases, the width of the bands near the Fermi level decreases. The width of some unoccupied bands close to the Fermi level finally decreases to an extremely small value (below 0.01 meV) when the twist angle is 4.58°. More and more flat bands appear as shown in Figure 2b as the twist angle decreases. The flat bands are well separated from other dispersed bands. When the twist angle is smaller than 3.47°, a series of flat bands also appear in the valence bands. The wave functions of flat bands at the Γ point are localized as shown in Figure 1h. The wave functions of occupied bands are localized at AB stacked zones (overlap of different types of atoms at the interface), while the wave functions of unoccupied bands are localized at AA stacked zones (overlap of identical types of atoms at the interface). The helicity of AA and AB zones are opposite. After atomic relaxation, AB zones expand, while AA zones shrink to a series of small dots. AA and AB zones form two well-arranged helical quantum dots, respectively. Interestingly, the helicity is well distinguished for electrons and holes. In each moiré superlattice, there are two equivalent AA stacked quantum dots. Thus, flat bands corresponding to AA zones are at least 2-fold degenerate. The two quantum dots localized at AA stacked zones form two sublattices (as shown in Figure 1h). There are two quantum dots in each moiré cell. There are a series of flat bands inside each site of a quantum dot. Above the Fermi level, the first state has an *s*-wave symmetry. The second and third states are degenerate, and they have p_x and p_y symmetries. Higher-energy flat bands have wave functions of *d*-wave envelope character, if the twist angle is small enough. The number of the degenerate flat bands matches the model of 2D

https://doi.org/10.1021/jacs.2c04390
J. Am. Chem. Soc. 2022, 144, 14657−14667

square quantum well.[7] These states are distributed inside a quantum dot with a size of around one nanometer.

In the limit of flat bands, the hopping term is zero. The effective Hamiltonian of materials can be written as (see details in the Methods)

$$H = \sum_{i,\alpha} E_\alpha c_{i,\alpha}^\dagger c_{i,\alpha} + \sum_{i\alpha,j\beta} U_{i,j} c_{i,\alpha}^\dagger c_{i,\alpha} c_{j,\beta}^\dagger c_{j,\beta} \quad (1)$$

where α and β indicate different orbitals inside a quantum dot. i and j are the different localization sites of the moiré pattern. The first term is the effective onsite energy of doped electrons. In our DFT calculations, even when the system is doped with electrons, the half-occupation does not lead to spin splitting. Thus, the effective Hubbard onsite term is zero. According to previous research, the DFT calcuations are exact enough to compute the magnetic ground state for flat bands, if the materials are magnetic.[55,56] The second term is the Coulomb interaction between different localization sites and can be approximated as $U_{ij} = \frac{e^2}{4\pi\varepsilon_0\varepsilon_r L}$, where L is the distance between two localized states. i and j are the indexes of localized states in real space. We include not only the nearest neighbor but also other terms of Coulomb interaction going beyond the nearest neighbor terms in real space. The quantity ε_0 is the vacuum dielectric constant. The relative permittivity ε_r of PbS nanosheet is 13.4 according to previous work.[57] The calculated value is 10.5 for bulk. Usually, 2D materials have an effective dielectric constant much smaller than the 3D bulk counterpart due to the lack of screening outside the 2D planes. The calculated dielectric constant of a monolayer PbS is found to be 1.9 in the in-plane direction and 1.1 in the direction perpendicular to the plane. In this work, we use an average of 1.6 as an estimation. The exchange part of Coulomb interaction is absent between different sites because the overlap of wave functions at different sites can be neglected. The electrons here are close to classical particles. The effective onsite energy E_α describes the energy when a doped electron occupies an orbital inside a localization site. The difference between different onsite energies is the excitation energy when an electron is excited from one orbital to another inside a site. Thus, the effective onsite energy can be fitted by the energy splitting of different flat bands and dispersed bands. The energy splitting as a function of twist angle is shown in Figure 2b. The energy separation between the conduction bands can be as large as 96 meV, when an electron is excited from the first flat band above the Fermi level to the second band. The excitation energy can be as large as 283 meV, when an electron is excited from the first conduction band to other bands with a large dispersion.

When the system is doped with a low electron concentration, the ground states of eq 1 are searched using the variational algorithm method (see the Methods). After electron doping, the electrons are distributed in a pattern to lower their total energy as shown in Figure 3. When the twist angle is large, the Coulomb interaction dominates over the onsite energy. To lower the Coulomb repulsive force, the electrons tend to occupy as many orbitals inside a site as possible and then keep a large distance with its neighbor-occupied states. The electrons will form a supercell even larger than the moiré cell. For example, Figure 3a–d shows results for when the system is doped with 144, 48, 24, or 23 electrons within a grid of 12 × 12 localized states.

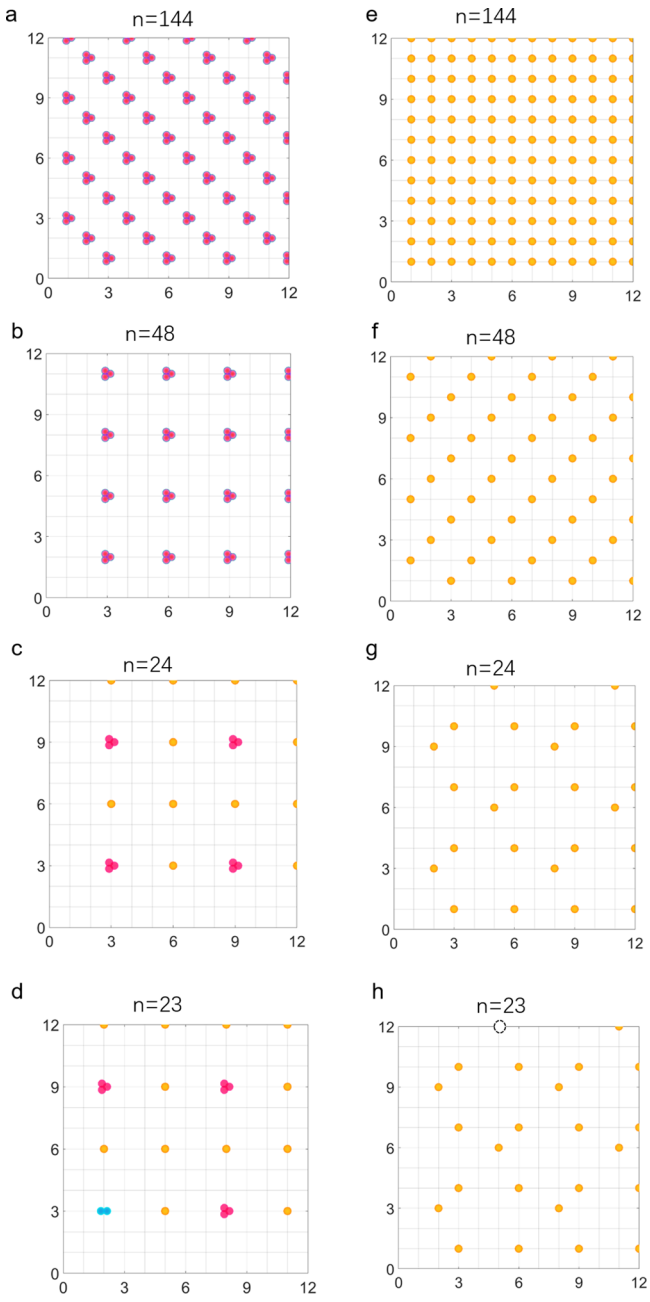

Figure 3. Phases of Wigner crystals. (a–d) Wigner crystals when 144, 48, 24, and 23 electrons are doped in a mesh of 12 × 12 quantum dots. The twist angle is 4.58°. Each crossing point represents a quantum dot. Colorful and solid dots represent occupied dots. Orange, blue, and red represent the occupation of 1, 2, and 3 inside a quantum dot, respectively. (e–h) Wigner crystals when 144, 48, 24, and 23 electrons are added in a mesh of 12 × 12 quantum dots. The twist angle is 2.66°.

As the twist angle decreases, the onsite term tends to be dominate. If the effective dielectric constant is 1.6, the estimated critical value is approximately 4°. When the twist angle is smaller than 4°, the onsite energy dominates over the Coulomb repulsion interaction. The electrons tend to occupy as many low-energy orbitals as possible and then lower the Coulomb repulsion interaction by keeping a large distance from its neighboring occupied state. For example, when the doped electron is 1.0 e/site, namely 144 electrons inside 12 × 12 localized states, the electrons will occupy all of the *s*-states

https://doi.org/10.1021/jacs.2c04390
J. Am. Chem. Soc. 2022, 144, 14657−14667

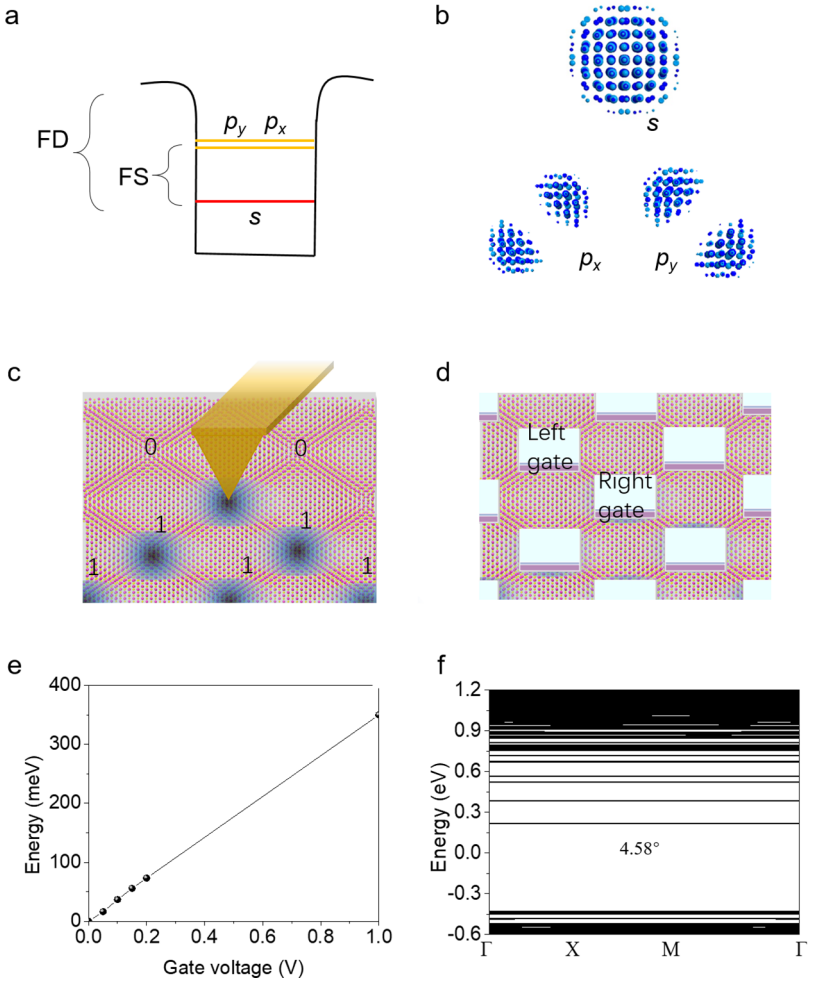

Figure 4. Localized states and devices. (a) Illustration of energy levels in a moiré quantum dot. The two *p* states are degenerate. A minor artificial splitting is to highlight the band number. (b) DFT-calculated wave functions of different flat bands. The twist angle is 4.58°. (c) Illustration of reading and writing in a memory device. (d) Illustration of controlling a memory device with gates. (e) Energy shift of a local *s*-state as a function of gate voltage. (f) Band structure of twisted PbS layers with gates. The gate voltage is +1 and −1 V on two neighboring localized states.

of all the sites as shown in Figure 3d. Some typical results of electron concentration are shown in Figure 3e−h. In some cases, the original translation symmetry and C_4 symmetry can spontaneously be broken. Since the quantum-well depth is large (up to 283 meV under some twist angles), the electron Wigner crystal is robust against thermal fluctuation. The Wigner crystal is stable probably at room temperature or even higher temperatures according to Maxwell−Boltzmann statistics. All these properties are beyond twisted bilayer graphene, whose energy separation between the two flat bands is only on the order of tens of meV.[58] Despite the possible existence of electron Wigner crystals in twisted bilayer graphene, it is only stable at a low temperature.[36]

When the twist angle decreases further, the excitation energy, especially excitation energy from the *s*-wave state to the dispersed states, further increases according to Figure 2b. This implies that the electrons are also difficult to scatter into the dispersed bands, even if the electron−electron interaction is turned on. In this case, electron Wigner lattices with a higher energy than the ground state can be prepared and are also stable. The observed electron distribution depends on the process of doping and annealing. As shown in Figure 4a,b, the deep local states are similar to artificial atoms. If some electrons are injected one by one as shown in Figure 4c, the electron will be trapped inside a square quantum dot formed by moiré superlattices. The localized states can work as a single-electron memory device. The charged quantum dots represent 1, and the neutral quantum dots represent 0. The signals can be read by the single-electron technique.[59] The localized states can be controlled by a gate as shown in Figure 4d. When a negative gate voltage is applied on a local state, the energy of the local state will be lifted. For example, two square gates are applied on two AA stacking points. Each gate has a dimension of $2 \times 2 \times 0.25$ nm^3. The dielectric layer is assumed as Al_2O_3, and the effective relative permittivity is 4. The energy shift of a local state is linearly proportional to the gate voltage as shown in Figure 4e. Roughly, the energy level lifts by 700 meV when the difference of two neighbor gate voltages increases by 2 V. The detailed band structures are shown in Figure S5. An example of a band structure with a left gate voltage of 1 V and a right gate voltage of −1 V is shown in Figure 4f. According to the wave functions, the several flat bands near the Fermi level belong to one of the AA stacking zones. The states of the other AA stacking zones inside a moiré supercell move above the dispersed states, and electrons will flow away from high-energy states toward low-energy local states. The regular quantum dot array in the PbS moiré superlattice may be useful for single-electron devices. The

https://doi.org/10.1021/jacs.2c04390
J. Am. Chem. Soc. 2022, 144, 14657−14667

device density can be as large as 25 per square nanometer, which is far beyond the current nonvolatile memory such as flash memory.

2.2. Experimental Synthesis. Non-vdW moiré superlattices are unusual, so their accessibility and stability may be controversial. In experiments, we used an aqueous synthesis strategy to grow nanosheets of PbS in solvents. Then ligands were removed by washing with dilute basic and acidic aqueous solutions. The naked PbS nanosheets are immediately drop-casted, and the moiré superlattices were assembled after the solvent evaporation (illustrated in Figure 5a). TEM imaging and statistics (Figure 5b,c) show that the nanosheets have a rectangular shape, with an average width and length of around 40 nm × 200 nm. A series of moiré superlattices with different twist angles are found in the overlap zones stacked by two nanosheets. We further perform the side-view imaging through a combination of focused ion beam (FIB) and TEM (Figure 5d,e). The side-view imaging shows that the nanosheets have a thickness distribution ranging from 3 to 10 nm, which corresponds to 10−34 atomic layers. More importantly, it reveals a direct contact at the interfaces of all overlapped nanosheets, validating the successful construction of non-vdW twisted superlattices.

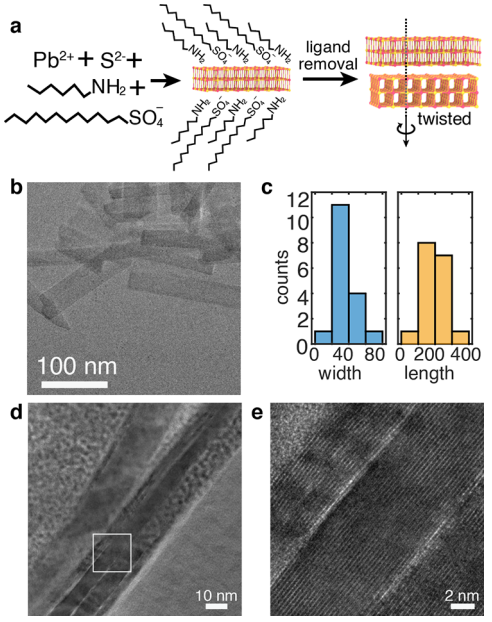

Figure 5. Synthesis and TEM characterization of PbS twisted layers. (a) Schematic of the synthetic procedure. (b) Low magnification TEM image showing the shape and size of PbS nanosheets. (c) Statistics of the width and length of nanosheets. (d) Side-view TEM image of twisted layers prepared through FIB. (e) Zoom-in of the boxed area in (d).

High-resolution top-view TEM images provide more structural details, enabling us to compare them with our calculations. Parts a−c of Figure 6 show the TEM analysis of an exemplary moiré superlattice with a twist angle of 7.90°. The FFT pattern (Figure 6c) shows that both sheets have the same rock-salt structure and align along the zone axis [001], showing two sets of C_4-symmetric patterns. The two sets of patterns have a tilted angle of 7.90°. This is how the twist angles of all superlattices are evaluated. We are especially interested in structures with small twist angles (Figure 6d,e) because according to our DFT calculations (shown in Figure 1) the superlattices with small twist angles should look like 2D arrays of identical quantum dots. As demonstrated in Figure 6e, the moiré superlattice with a 2.66° twist angle consists of periodic AA/AB regions arranged in the square symmetry and indeed resembles an epitaxially fused superlattice of quantum dots. The lattice constant is about 13.7 nm. Some strained moiré superlattices with strains are found during synthesis (Figures S6 and S7). The statistics of twist angles (Figure 6f) suggest that twisted bilayers formed through drop-casting have an average twist angle (12.6°), which is smaller than the random distribution (22.5°), probably due to the strong PbS−PbS interfacial interaction. Unfortunately, due to the technical challenges in the resolution of vertical atomic positions in the nanosheets, it is hard to extract the strain vortices at the interface experimentally.

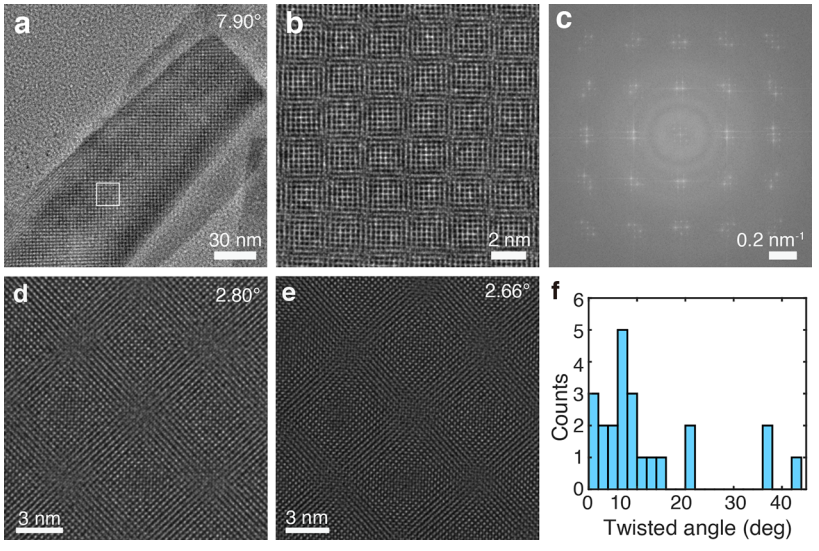

Figure 6. TEM images of moiré superlattices. (a) Overview TEM image. (b) Zoom-in image of boxed area in (a). (c) FFT pattern of (b). Twist angle measured from the two sets of C_4 symmetric patterns is 7.90°. (d,e) Atomic-resolution TEM images of moiré superlattices with two small twist angles. (f) Statistics of the twist angles in moiré superlattices through analysis of high-resolution TEM images.

https://doi.org/10.1021/jacs.2c04390
J. Am. Chem. Soc. 2022, 144, 14657−14667

3. METHODS

Synthesis and Sample Preparation. PbS nanosheets were synthesized by mixing a 10 mL aqueous solution of lead acetate (20 mM), thioacetamide (20 mM), formic acid (0.3 M), sodium dodecyl sulfate (1 mM), and hexylamine (5 mM) at 100 °C for 20 min. The obtained sample was centrifuged and washed at least three times with sodium hydroxide solution, formic acid solution (10 mM, 1 mL), and water (1 mL) sequentially. The colloid solution of nanosheets was then immediately drop-casted onto holey-carbon TEM grids. Grids with PbS moiré superlattices were heated at 100 °C in a vacuum for 6 h. The morphology of the moiré superlattices was investigated by the FEI Them IS aberration-corrected TEM at the Molecular Foundry at Lawrence Berkeley National Laboratory. Samples for FIB were prepared by drop-casting nanosheets onto a silicon substrate and then cut into thin slices by Ga beam in a Helios Dual Beam system. The thin slices were transferred into TEM holders and measured by FEI ThemIS. More details about the synthetization and characterization can be found in our previous experimental work on the synthesis and optical characterization.[23]

Density Functional Theory Calculations. The calculations of density functional theory were performed using a single-ζ atomic basis set and PBE exchange-correlation functional. The pseudopotential of FHI is applied. DFT-D2 is applied to include the interlayer molecular interaction. Due to the large lattice length, a 1 × 1 × 1 k-mesh is used when the twist angle is below 4.58°. Density-mesh is cut off at 80 hartrees. The spin−orbital coupling is neglected. The atomic positions in the twisted structures are relaxed until the force on each atom is smaller than 0.01 eV/Å. We tested the GGA+U method with nonzero U for the structure with a big twist angles above 4.58°, and there is no significant difference.

Extended Hubbard Hamilton of Flat Bands. Generally, the Hamiltonian for the multiband Hubbard model is written as

$$H = \sum_{i\sigma} E_{i\sigma} c_{i\sigma}^{\dagger} c_{i\sigma} + \sum_{\langle ij\rangle\sigma} t_{ij} c_{i\sigma}^{\dagger} c_{j\sigma} + \sum_{i\sigma} U_i c_{i\uparrow}^{\dagger} c_{i\uparrow} c_{i\downarrow}^{\dagger} c_{i\downarrow} + \sum_{ij\sigma\sigma'} U_{ij} c_{i\sigma}^{\dagger} c_{i\sigma} c_{j\sigma'}^{\dagger} c_{j\sigma'} \quad (2)$$

where $E_{i\sigma}$ is the single-electron onsite energy. t_{ij} is the hopping integration, U_i is the onsite two-electron Coulomb repulsive interaction, and U_{ij} is the neighbor electron−electron interaction. σ and σ' represent spin and run over $\{\uparrow, \downarrow\}$. In the DFT calculations, the effect of the first and second terms are naturally included. The third and fourth terms are partially included, although the single-electron approximation is applied.[60]

$$E_i = \int \varphi_i^*(r)\left(\frac{\hbar^2\nabla^2}{-2m_e} + V(r)\right)\varphi_i(r)\, \mathrm{d}r^3 \quad (3)$$

$$t_{ij} = \int \varphi_i^*(r)\left(\frac{\hbar^2\nabla^2}{-2m_e} + V(r)\right)\varphi_j(r)\, \mathrm{d}r^3 \quad (4)$$

$$U_{ij,kl} = \frac{e^2}{4\pi\varepsilon_0}\int\int \mathrm{d}r_1^3\, \mathrm{d}r_2^3 \frac{\varphi_i^*(r_1)\varphi_j^*(r_2)\varphi_l(r_2)\varphi_k(r_1)}{|r_1 - r_2|} \quad (5)$$

For simplification, the spin and orbital indexes have been absorbed in the index i, j, k, and l.

Using this, we map the electronic states near the Fermi level in PbS moiré superlattices to an effective multiband Hubbard model. For highly localized states (flat bands), we can set t_{ij} to zero. U_i is the repulsion energy when two electrons with opposite spins occupy one state. We can use the spin-polarized DFT method to calculate the energy difference when a localized state is doped with one and two electrons. The calculated energy differences of the localized states are small, which indicates U_i is close to 0. In physics, if U_i is large enough, the materials will undergo a spin splitting according to Stoner criteria, when a flat band is half occupied (one electron in one flat band when the spin channel is open).[61−64] Then the spin splitting of a flat band is equal to U_i for the corresponding localized state at a site. We perform the DFT calculation with one doped electron. In this case, the first band above the Fermi level is half occupied considering spin, but there is no spin splitting. This is another evidence for $U_i \approx 0$. To avoid a possible calculation error, we followed a previous DFT calculation of $Sn_2Ta_2O_7$[65] and found a spin splitting when the flat band is half occupied. Thus, we confirm that the effective U_i is small and can be neglected for the fat bands above the Fermi level in PbS moiré superlattices. At least, the effective U_i is much smaller than the flat-band separation. A small onsite Coulomb repulsion energy is possibly due to the large screening inside a localized state. Actually, the onsite Coulomb repulsive energy estimated by other methods is not large in many other twisted bilayer materials.[66] One can further reduce the onsite Coulomb interaction by placing an metal electrode on top of the "quantum dot" to enhance the screening. Thus, in the following, we will ignore the onsite Coulomb interaction term.

For the last term, the classical part of Coulomb interaction is

$$U_{i\sigma j\sigma'} = \frac{e^2}{4\pi\varepsilon_0}\int\int \mathrm{d}r_1^3\, \mathrm{d}r_2^3 \frac{\varphi_{i\sigma}^*(r_1)\varphi_{j\sigma'}^*(r_2)\varphi_{j\sigma'}(r_2)\varphi_{i\sigma}(r_1)}{|r_1 - r_2|}$$

and the exchange term is

$$U_{i\sigma j\sigma'}^{ex} = \frac{e^2}{4\pi\varepsilon_0}\int\int \mathrm{d}r_1^3 \mathrm{d}r_2^3 \frac{\varphi_{i\sigma}^*(r_1)\varphi_{j\sigma'}^*(r_2)\varphi_{j\sigma'}(r_1)\varphi_{i\sigma}(r_2)}{|r_1 - r_2|}$$

Since there is no overlap between the two neighboring sites, $\varphi_{i\sigma}^*(r_1)\varphi_{j\sigma'}(r_1) = \varphi_{j\sigma'}^*(r_2)\varphi_{i\sigma}(r_2) = 0$ everywhere. Thus, there is no exchange interaction. The last term in eq 2 only includes the classical Coulomb interaction and can be approximated as $U_{ij} = \frac{e^2}{4\pi\varepsilon_0\varepsilon_r L} = 1.439\ \mathrm{eV\,nm}/\varepsilon_r L$, where L is the distance between two localized states. i and j are the indexes of localized states in real space. The effective Hamiltonian is written as eq 1. We use not only the nearest neighbor terms but also other terms of Coulomb interactions beyond the nearest neighbor in real space.

This is different from twisted bilayer graphene. When the twist angle is close to the magic angle, the bandwidth near the Fermi level is still not zero. The possible onsite interaction in the third term in eq 2 can be non-zero. Further, the exchange interaction in the fourth term in eq 2 is non-zero because $\varphi_{i\sigma}^*(r_1)\varphi_{j\sigma'}(r_1)$ and $\varphi_{j\sigma'}^*(r_2)\varphi_{i\sigma}(r_2)$ can be nonzero. The magnetic properties can be observed in twisted bilayer graphene.[67,68]

Please note the U_i and U_{ij} for artificial quantum dots are different from the U in the GGA+U method of DFT, although they have a hidden relationship with each other. The U in GGA+U aims to correct the possible correlated interaction for the atomic orbitals. The U_i and U_{ij} in our extended Hubbard model are the effective two-electron interactions for the localized states in moiré superlattices.

Numerical Solutions of Wigner Crystals. The ground states of eq 1 are explored using the variational algorithm method. For a certain twisted structure, we know the orbital number of localized (N_{or}) in an artificial quantum dot in a moiré superlattice based on the DFT-calculated band structures. We assume the electrons in the dispersed bands can freely propagate in the real space. For example, there are three localized states ($N_{or} = 3$) in a twisted structure with a twist angle of 4.58°, and all other states above the Fermi level can freely propagate in real space. Each quantum dot hosts a maximum electron number of N_{or} without including spin. Then we determine the static energy of each orbital and all the Coulomb repulsion interactions in eq 1. For the same example with a twist angle of 4.58°, the single-electron onsite energy is $E_s = -0.158$ eV, $E_{px} = E_{py} = -0.057$ eV. Each AA stacking zone is treated as an artificial quantum dot. We use a 12 × 12 superlattice mesh of artificial quantum dots to host the doped electrons. Then we doped the desired number (n_e) of electrons in the mesh. When the n_e electrons occupy different orbitals at different sites, the system energy is the sum of all electrons' orbital energy and the Coulomb repulsion energy between any two electrons at different sites. By changing the occupation of orbitals at each site of the 12 × 12 mesh, the occupation configuration with the minimum energy is the desired ground state of the Wigner crystals. The self-

https://doi.org/10.1021/jacs.2c04390
J. Am. Chem. Soc. 2022, 144, 14657−14667

developed code is performed to search the ground states of the Wigner crystals based on the above algorithm.

4. CONCLUSIONS

In the previous literature, moiré superlattices are mainly stacked by twisted 2D vdW layer materials. Here we synthesized non-vdW material moiré superlattices. TEM observations confirmed the twisted PbS layers with interlayer chemical bonds. The structure is similar to the square matrices of quantum dots. Theoretically, we found the strong interlayer coupling leads to giant chiral strain and dipole vortices at the interface. The calculated electronic structures of twisted structures show a series of ultraflat bands with atom-like wave functions, which are also like quantum dots on the nanoscale. Our calculations suggest that if the twisted PbS layers are doped with a low concentration of electrons then different phases of Wigner crystallinity will spontaneously form according to numerical simulation.

■ ASSOCIATED CONTENT

Supporting Information

The Supporting Information is available free of charge at https://pubs.acs.org/doi/10.1021/jacs.2c04390.

Additional calculation results and experimental details including band gap versus atomic number, atomic displacement in twisted nanosheets, band structure of a single nanosheet with a vortex strain, band edge energy as a function of an interlayer shift, band structures controlled by gates, TEM images of moiré superlattices under asymmetric strain, and free energy of monolayer PbS as a function of strain in the *y*-direction (PDF)

■ AUTHOR INFORMATION

Corresponding Authors

Prineha Narang − *John A. Paulson School of Engineering and Applied Sciences, Harvard University, Cambridge, Massachusetts 02138, United States;* orcid.org/0000-0003-3956-4594; Email: prineha@seas.harvard.edu

Lin-Wang Wang − *State Key Laboratory of Superlattices and Microstructures, Institute of Semiconductors, Chinese Academy of Sciences, Beijing 100083, China;* orcid.org/0000-0001-7061-2692; Email: lwwang@semi.ac.cn

Authors

Zhigang Song − *John A. Paulson School of Engineering and Applied Sciences, Harvard University, Cambridge, Massachusetts 02138, United States;* orcid.org/0000-0002-8355-6498

Yu Wang − *South China Advanced Institute for Soft Matter Science and Technology, School of Emergent Soft Matter, South China University of Technology, Guangzhou 510640, China*

Haimei Zheng − *Materials Sciences Division, Lawrence Berkeley National Laboratory, Berkeley, California 94720, United States; Department of Materials Science and Engineering, University of California, Berkeley, California 94720, United States;* orcid.org/0000-0003-3813-4170

Complete contact information is available at: https://pubs.acs.org/10.1021/jacs.2c04390

Author Contributions

#Z.S. and Y.W. contributed equally to this work.

Notes

The authors declare no competing financial interest.

■ ACKNOWLEDGMENTS

This work is partially supported by the Office of Naval Research (ONR) MURI Program under Grant NO. ONR N00014-21-1-2537 as well as the by the U.S. Department of Energy, Office of Science, Basic Energy Sciences (BES), Materials Sciences and Engineering Division under FWP ERKCK47 'Understanding and Controlling Entangled and Correlated Quantum States in Confined Solid-state Systems Created via Atomic Scale Manipulation' (spin qubits), and by the Army Research Office MURI (Ab Initio Solid-State Quantum Materials) Grant No. W911NF-18-1-0431 (computational methods for low dimensional materials). P.N. acknowledges support as a Moore Inventor Fellow through Grant No. GBMF8048 and gratefully acknowledges support from the Gordon and Betty Moore Foundation as well as support from a NSF CAREER Award under Grant No. NSF-ECCS-1944085. H.Z. acknowledge the support by the DOE, Office of Science, Office of BES, Materials Sciences and Engineering Division under Contract No. 415 DE-AC02-05-CH11231 within the KC22ZH program.

■ REFERENCES

(1) Zhang, X.; Li, H.-O.; Wang, K.; Cao, G.; Xiao, M.; Guo, G.-P. Qubits Based on Semiconductor Quantum Dots. *Chin. Phys. B* **2018**, *27*, 020305.

(2) Lv, Z.; Wang, Y.; Chen, J.; Wang, J.; Zhou, Y.; Han, S.-T. Semiconductor Quantum Dots for Memories and Neuromorphic Computing Systems. *Chem. Rev.* **2020**, *120*, 3941.

(3) Arakawa, Y.; Holmes, M. J. Progress in Quantum-Dot Single Photon Sources for Quantum Information Technologies: A Broad Spectrum Overview. *Appl. Phys. Rev.* **2020**, *7*, 021309.

(4) Whitham, K.; Yang, J.; Savitzky, B. H.; Kourkoutis, L. F.; Wise, F.; Hanrath, T. Charge Transport and Localization in Atomically Coherent Quantum Dot Solids. *Nat. Mater.* **2016**, *15*, 557.

(5) Kagan, C. R.; Murray, C. B. Charge Transport in Strongly Coupled Quantum Dot Solids. *Nat. Nanotechnol.* **2015**, *10*, 1013.

(6) Naik, M. H.; Kundu, S.; Maity, I.; Jain, M. Origin and Evolution of Ultraflat Bands in Twisted Bilayer Transition Metal Dichalcogenides: Realization of Triangular Quantum Dots. *Phys. Rev. B* **2020**, *102*, 075413.

(7) Song, Z.; Sun, X.; Wang, L. Switchable Asymmetric Moire Patterns with Strongly Localized States. *J. Phys. Chem. Lett.* **2020**, *11*, 9224.

(8) Kennes, D. M.; Claassen, M.; Xian, L.; Georges, A.; Millis, A. J.; Hone, J.; Dean, C. R.; Basov, D.; Pasupathy, A. N.; Rubio, A. Moiré Heterostructures as a Condensed-Matter Quantum Simulator. *Nat. Phys.* **2021**, *17*, 155.

(9) Tang, Y.; Li, L.; Li, T.; Xu, Y.; Liu, S.; Barmak, K.; Watanabe, K.; Taniguchi, T.; MacDonald, A. H.; Shan, J. Simulation of Hubbard Model Physics in WSe_2/WS_2 Moiré Superlattices. *Nature* **2020**, *579*, 353.

(10) Naik, M. H.; Jain, M. Ultraflatbands and Shear Solitons in Moiré Patterns of Twisted Bilayer Transition Metal Dichalcogenides. *Phys. Rev. Lett.* **2018**, *121*, 266401.

(11) Xian, L.; Claassen, M.; Kiese, D.; Scherer, M. M.; Trebst, S.; Kennes, D. M.; Rubio, A. Realization of Nearly Dispersionless Bands with Strong Orbital Anisotropy from Destructive Interference in Twisted Bilayer MoS_2. *Nat. Commun.* **2021**, *12*, 1.

(12) Carr, S.; Fang, S.; Zhu, Z.; Kaxiras, E. Exact Continuum Model for Low-Energy Electronic States of Twisted Bilayer Graphene. *Phys. Rev. Res.* **2019**, *1*, 013001.

(13) Lucignano, P.; Alfè, D.; Cataudella, V.; Ninno, D.; Cantele, G. Crucial Role of Atomic Corrugation on the Flat Bands and Energy

Gaps of Twisted Bilayer Graphene at the Magic Angle Θ∼1. 08°. *Phys. Rev. B* **2019**, *99*, 195419.
(14) Zhang, Y.; Zhan, Z.; Guinea, F.; Silva-Guillén, J. Á.; Yuan, S. Tuning Band Gaps in Twisted Bilayer MoS_2. *Phys. Rev. B* **2020**, *102*, 235418.
(15) Angeli, M.; MacDonald, A. H. Γ Valley Transition Metal Dichalcogenide Moiré Bands. *Proc. Natl. Acad. Sci. U.S.A.* **2021**, *118*, e2021826118.
(16) Tran, K.; Moody, G.; Wu, F.; Lu, X.; Choi, J.; Kim, K.; Rai, A.; Sanchez, D. A.; Quan, J.; Singh, A. Evidence for Moiré Excitons in Van Der Waals Heterostructures. *Nature* **2019**, *567*, 71.
(17) Li, Y.; Dietrich, S.; Forsythe, C.; Taniguchi, T.; Watanabe, K.; Moon, P.; Dean, C. R. Anisotropic Band Flattening in Graphene with One-Dimensional Superlattices. *Nat. Nanotechnol.* **2021**, *16*, 525.
(18) Huang, X.; Wang, T.; Miao, S.; Wang, C.; Li, Z.; Lian, Z.; Taniguchi, T.; Watanabe, K.; Okamoto, S.; Xiao, D. Correlated Insulating States at Fractional Fillings of the WS_2/WSe_2 Moiré Lattice. *Nat. Phys.* **2021**, *17*, 715.
(19) Wang, L.; Shih, E.-M.; Ghiotto, A.; Xian, L.; Rhodes, D. A.; Tan, C.; Claassen, M.; Kennes, D. M.; Bai, Y.; Kim, B. Correlated Electronic Phases in Twisted Bilayer Transition Metal Dichalcogenides. *Nat. Mater.* **2020**, *19*, 861.
(20) Wong, D.; Nuckolls, K. P.; Oh, M.; Lian, B.; Xie, Y.; Jeon, S.; Watanabe, K.; Taniguchi, T.; Bernevig, B. A.; Yazdani, A. Cascade of Electronic Transitions in Magic-Angle Twisted Bilayer Graphene. *Nature* **2020**, *582*, 198.
(21) Cao, Y.; Fatemi, V.; Fang, S.; Watanabe, K.; Taniguchi, T.; Kaxiras, E.; Jarillo-Herrero, P. Unconventional Superconductivity in Magic-Angle Graphene Superlattices. *Nature* **2018**, *556*, 43.
(22) Cao, Y.; Fatemi, V.; Demir, A.; Fang, S.; Tomarken, S. L.; Luo, J. Y.; Sanchez-Yamagishi, J. D.; Watanabe, K.; Taniguchi, T.; Kaxiras, E. Correlated Insulator Behaviour at Half-Filling in Magic-Angle Graphene Superlattices. *Nature* **2018**, *556*, 80.
(23) Wang, Y.; Song, Z.; Wan, J.; Betzler, S.; Xie, Y.; Ophus, C.; Bustillo, K.; Ercius, P.; Wang, L.-w; Zheng, H. Strong structural and electronic coupling in metavalent PbS moire superlattice. *arXiv* July 25, **2022**, , https://arxiv.org/pdf/2207.11106v1.pdf (accessed 2022-07-25).
(24) Shabani, S.; Halbertal, D.; Wu, W.; Chen, M.; Liu, S.; Hone, J.; Yao, W.; Basov, D. N.; Zhu, X.; Pasupathy, A. N. Deep Moiré Potentials in Twisted Transition Metal Dichalcogenide Bilayers. *Nat. Phys.* **2021**, *17*, 720.
(25) Alden, J. S.; Tsen, A. W.; Huang, P. Y.; Hovden, R.; Brown, L.; Park, J.; Muller, D. A.; McEuen, P. L. Strain Solitons and Topological Defects in Bilayer Graphene. *Proc. Natl. Acad. Sci. U.S.A.* **2013**, *110*, 11256.
(26) Gadelha, A. C.; Ohlberg, D. A.; Rabelo, C.; Neto, E. G.; Vasconcelos, T. L.; Campos, J. L.; Lemos, J. S.; Ornelas, V.; Miranda, D.; Nadas, R. Localization of Lattice Dynamics in Low-Angle Twisted Bilayer Graphene. *Nature* **2021**, *590*, 405.
(27) Kazmierczak, N. P.; Van Winkle, M.; Ophus, C.; Bustillo, K. C.; Carr, S.; Brown, H. G.; Ciston, J.; Taniguchi, T.; Watanabe, K.; Bediako, D. K. Strain Fields in Twisted Bilayer Graphene. *Nat. Mater.* **2021**, *20*, 956.
(28) Quan, J.; Linhart, L.; Lin, M.-L.; Lee, D.; Zhu, J.; Wang, C.-Y.; Hsu, W.-T.; Choi, J.; Embley, J.; Young, C. Phonon Renormalization in Reconstructed MoS_2 Moiré Superlattices. *Nat. Mater.* **2021**, *20*, 1100.
(29) Kumar, O.; Kaur, M. Single Electron Transistor: Applications & Problems. *Int. J. VLSI Des Commun. Syst. (VLSICS)* **2010**, *1*, 24.
(30) Kubatkin, S.; Danilov, A.; Hjort, M.; Cornil, J.; Bredas, J.-L.; Stuhr-Hansen, N.; Hedegård, P.; Bjørnholm, T. Single-Electron Transistor of a Single Organic Molecule with Access to Several Redox States. *Nature* **2003**, *425*, 698.
(31) Liu, Z.; Liu, F.; Wu, Y.-S. Exotic Electronic States in the World of Flat Bands: From Theory to Material. *Chin. Phys. B* **2014**, *23*, 077308.
(32) Wigner, E. On the Interaction of Electrons in Metals. *Phys. Rev.* **1934**, *46*, 1002.
(33) Shapir, I.; Hamo, A.; Pecker, S.; Moca, C.; Legeza, Ö.; Zarand, G.; Ilani, S. Imaging the Electronic Wigner Crystal in One Dimension. *Science* **2019**, *364*, 870.
(34) Zhou, Y.; Sung, J.; Brutschea, E.; Esterlis, I.; Wang, Y.; Scuri, G.; Gelly, R. J.; Heo, H.; Taniguchi, T.; Watanabe, K.; Zaránd, G.; Lukin, M. D.; Kim, P.; Demler, E.; Park, H. Bilayer Wigner Crystals in a Transition Metal Dichalcogenide Heterostructure. *Nature* **2021**, *595*, 48.
(35) Smoleński, T.; Dolgirev, P. E.; Kuhlenkamp, C.; Popert, A.; Shimazaki, Y.; Back, P.; Lu, X.; Kroner, M.; Watanabe, K.; Taniguchi, T.; Esterlis, I.; Demler, E.; Imamoğlu, A. Signatures of Wigner Crystal of Electrons in a Monolayer Semiconductor. *Nature* **2021**, *595*, 53.
(36) Padhi, B.; Setty, C.; Phillips, P. W. Doped Twisted Bilayer Graphene near Magic Angles: Proximity to Wigner Crystallization, Not Mott Insulation. *Nano Lett.* **2018**, *18*, 6175.
(37) Smoleński, T.; Dolgirev, P. E.; Kuhlenkamp, C.; Popert, A.; Shimazaki, Y.; Back, P.; Lu, X.; Kroner, M.; Watanabe, K.; Taniguchi, T. Signatures of Wigner Crystal of Electrons in a Monolayer Semiconductor. *Nature* **2021**, *595*, 53.
(38) Jang, J.; Hunt, B. M.; Pfeiffer, L. N.; West, K. W.; Ashoori, R. C. Sharp Tunnelling Resonance from the Vibrations of an Electronic Wigner Crystal. *Nat. Phys.* **2017**, *13*, 340.
(39) Abbas, G.; Li, Y.; Wang, H.; Zhang, W. X.; Wang, C.; Zhang, H. Recent Advances in Twisted Structures of Flatland Materials and Crafting Moiré Superlattices. *Adv. Funct. Mater.* **2020**, *30*, 2000878.
(40) Song, Z.; Sun, X.; Wang, L.-W. Eshelby-Twisted Three-Dimensional Moiré Superlattices. *Phys. Rev. B* **2021**, *103*, 245206.
(41) Carr, S.; Fang, S.; Kaxiras, E. Electronic-Structure Methods for Twisted Moiré Layers. *Nat. Rev. Mater.* **2020**, *5*, 748.
(42) Halbertal, D.; Finney, N. R.; Sunku, S. S.; Kerelsky, A.; Rubio-Verdú, C.; Shabani, S.; Xian, L.; Carr, S.; Chen, S.; Zhang, C. Moiré Metrology of Energy Landscapes in Van Der Waals Heterostructures. *Nat. Commun.* **2021**, *12*, 1.
(43) Weston, A.; Zou, Y.; Enaldiev, V.; Summerfield, A.; Clark, N.; Zólyomi, V.; Graham, A.; Yelgel, C.; Magorrian, S.; Zhou, M. Atomic Reconstruction in Twisted Bilayers of Transition Metal Dichalcogenides. *Nat. Nanotechnol.* **2020**, *15*, 592.
(44) McGilly, L. J.; Kerelsky, A.; Finney, N. R.; Shapovalov, K.; Shih, E.-M.; Ghiotto, A.; Zeng, Y.; Moore, S. L.; Wu, W.; Bai, Y. Visualization of Moiré Superlattices. *Nat. Nanotechnol.* **2020**, *15*, 580.
(45) Jung, J.; Laksono, E.; DaSilva, A. M.; MacDonald, A. H.; Mucha-Kruczyński, M.; Adam, S. Moiré Band Model and Band Gaps of Graphene on Hexagonal Boron Nitride. *Phys. Rev. B* **2017**, *96*, 085442.
(46) Batsanov, S. S. Van Der Waals Radii of Elements. *Inorg. Mater.* **2001**, *37*, 871.
(47) Lee, K.; Murray, É. D.; Kong, L.; Lundqvist, B. I.; Langreth, D. C. Higher-Accuracy Van Der Waals Density Functional. *Phys. Rev. B* **2010**, *82*, 081101.
(48) Chakarova-Käck, S. D.; Schröder, E.; Lundqvist, B. I.; Langreth, D. C. Application of Van Der Waals Density Functional to an Extended System: Adsorption of Benzene and Naphthalene on Graphite. *Phys. Rev. Lett.* **2006**, *96*, 146107.
(49) Nagaosa, N.; Tokura, Y. Topological Properties and Dynamics of Magnetic Skyrmions. *Nat. Nanotechnol.* **2013**, *8*, 899.
(50) Yadav, A.; Nelson, C.; Hsu, S.; Hong, Z.; Clarkson, J.; Schlepütz, C.; Damodaran, A.; Shafer, P.; Arenholz, E.; Dedon, L. Observation of Polar Vortices in Oxide Superlattices. *Nature* **2016**, *530*, 198.
(51) Jia, C.-L.; Urban, K. W.; Alexe, M.; Hesse, D.; Vrejoiu, I. Direct Observation of Continuous Electric Dipole Rotation in Flux-Closure Domains in Ferroelectric Pb (Zr, Ti) O_3. *Science* **2011**, *331*, 1420.
(52) Gregg, J. Exotic Domain States in Ferroelectrics: Searching for Vortices and Skyrmions. *Ferroelectrics* **2012**, *433*, 74.
(53) Tong, Q.; Chen, M.; Xiao, F.; Yu, H.; Yao, W. Interferences of Electrostatic Moiré Potentials and Bichromatic Superlattices of Electrons and Excitons in Transition Metal Dichalcogenides. *2D Mater.* **2021**, *8*, 025007.

https://doi.org/10.1021/jacs.2c04390
J. Am. Chem. Soc. 2022, 144, 14657−14667

(54) Zhang, C.; Chuu, C.-P.; Ren, X.; Li, M.-Y.; Li, L.-J.; Jin, C.; Chou, M.-Y.; Shih, C.-K. Interlayer Couplings, Moiré Patterns, and 2D Electronic Superlattices in MoS_2/WSe_2 Hetero-Bilayers. *Sci. Adv.* **2017**, *3*, e1601459.
(55) Hase, I.; Yanagisawa, T.; Kawashima, K. Flat-Band in Pyrochlore Oxides: A First-Principles Study. *Nanomater.* **2019**, *9*, 876.
(56) Yamada, M. G.; Soejima, T.; Tsuji, N.; Hirai, D.; Dincă, M.; Aoki, H. First-Principles Design of a Half-Filled Flat Band of the Kagome Lattice in Two-Dimensional Metal-Organic Frameworks. *Phys. Rev. B* **2016**, *94*, 081102.
(57) Khan, A. H.; Pal, S.; Dalui, A.; Pradhan, J.; Sarma, D.; Acharya, S. Solution-Processed Free-Standing Ultrathin Two-Dimensional Pbs Nanocrystals with Efficient and Highly Stable Dielectric Properties. *Chem. Mater.* **2017**, *29*, 1175.
(58) Tarnopolsky, G.; Kruchkov, A. J.; Vishwanath, A. Origin of Magic Angles in Twisted Bilayer Graphene. *Phys. Rev. Lett.* **2019**, *122*, 106405.
(59) Kataoka, M.; Astley, M.; Thorn, A.; Oi, D.; Barnes, C.; Ford, C.; Anderson, D.; Jones, G.; Farrer, I.; Ritchie, D. Coherent Time Evolution of a Single-Electron Wave Function. *Phys. Rev. Lett.* **2009**, *102*, 156801.
(60) Nolting, W.; Brewer, W. D. *Fundamentals of Many-Body Physics*; Springer, 2008; pp 37−64.
(61) Stoner, E. C. Collective Electron Ferromagnetism. *Proc. R Soc. London A Math. Phys. Sci.* **1938**, *165*, 372.
(62) Shastry, B.; Krishnamurthy, H.; Anderson, P. Instability of the Nagaoka Ferromagnetic State of the U = ∞ Hubbard Model. *Phys. Rev. B* **1990**, *41*, 2375.
(63) Fernando, G.; Kocharian, A.; Watson, R.; Weinert, M. Stoner Criterion of Ferromagnetism and Moment Saturation in the Hubbard Model with an Applied Magnetic Field. *Phys. B: Condens. Matter* **1997**, *230*, 509.
(64) Mielke, A.; Tasaki, H. Ferromagnetism in the Hubbard Model. *Commun. Math. Phys.* **1993**, *158*, 341.
(65) Hase, I.; Yanagisawa, T.; Aiura, Y.; Kawashima, K. Possibility of Flat-Band Ferromagnetism in Hole-Doped Pyrochlore Oxides $Sn_2Nb_2O_7$ and $Sn_2Ta_2o_7$. *Phys. Rev. Lett.* **2018**, *120*, 196401.
(66) Xu, Q.; Guo, Y.; Xian, L. Moiré Flat Bands in Twisted 2D Hexagonal Vdw Materials. *2D Mater.* **2022**, *9*, 014005.
(67) Gonzalez-Arraga, L. A.; Lado, J.; Guinea, F.; San-Jose, P. Electrically Controllable Magnetism in Twisted Bilayer Graphene. *Phys. Rev. Lett.* **2017**, *119*, 107201.
(68) Repellin, C.; Dong, Z.; Zhang, Y.-H.; Senthil, T. Ferromagnetism in Narrow Bands of Moiré Superlattices. *Phys. Rev. Lett.* **2020**, *124*, 187601.

https://doi.org/10.1021/jacs.2c04390
J. Am. Chem. Soc. 2022, 144, 14657−14667